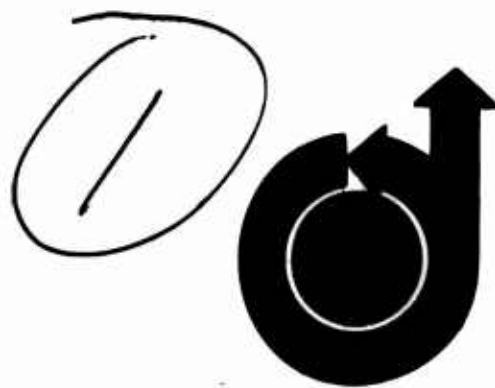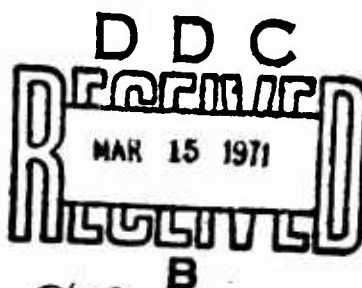# AIAA Paper No.68-1153
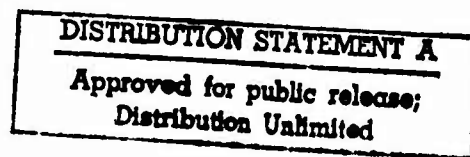
GRAPHITE ABLATION IN HIGH-PRESSURE ENVIRONMENTS

by

K. M. KRATSCH, M. R. MARTINEZ, F. I. CLAYTON, R. B. GREENE
and J. E. WUERER
McDonnell Douglas Astronautics Company – Western Division
Santa Monica, California

D D C

MAR 15 1971

B

AIAA Entry Vehicle Systems and Technology Meeting

WILLIAMSBURG, VIRGINIA/DECEMBER 3-5, 1968

GRAPHITE ABLATION IN HIGH-PRESSURE ENVIRONMENTS

K. M. Kratsch, M. R. Martinez, F. I. Clayton,
R. B. Greene, and J. E. Wuerer
Advance Aero/Thermodynamics and Nuclear Technology Department
Research and Development Directorate
Advance Systems and Technology
McDonnell Douglas Astronautics Company - Western Division
Santa Monica, California

Abstract

A performance analysis of the thermochemical/thermomechanical behavior of graphite is made extending present analysis procedures to include the allotropic features of bulk graphite. The analysis comprises a complete definition of graphite sublimation, and formulates a model for mechanical erosion based on erosion of individual grains. Newly computed thermodynamic functions for the polyatomic ring and chain carbon-molecules are used to define the sublimation regime; the probable uncertainty in these functions on computed vapor pressure and mass transfer is evaluated. Removal of graphite filler grains owing to preferential erosion of the binder matrix is described; numerical results are presented for the fraction of solid material mechanically eroded from the surface. Models fabricated from graphites encompassing fine- to coarse-grain filler particles were tested over a wide environmental spectrum. The high-pressure test data are correlated to establish the creditability of the analysis procedure. The composite effect of thermochemical and thermomechanical erosion is depicted in the test data correlations.

Notation

c	Velocity of light
c_i	Coefficient of ith atomic orbital in the molecular orbital of energy ϵ
C	Specific heat (condensed phase)
C_n	n^{th} carbon molecule
C_p	Specific heat of gas at constant pressure $\overline{C}_p = \left[\sum_j C_{p_j} K_j \right]$
C_H	Blowing value of Stanton number
C_{H_o}	Nonblowing value of Stanton number
D	Binary diffusion coefficient
E	Activation energy
E_i	Internal energy per interior carbon atom
f	Weight fraction
F^o	Standard free energy
ΔF_F^o	Standard free energy of formation
h	Height of exposed filler particle prior to recession
$\overline{h}$	Characteristic dimension of filler particle
H	Enthalpy; sum of sensible and chemical referenced to absolute zero temperature
H_{ii}	Coulomb integral of ith atomic orbital
H_{ij}	Resonance integral by i^{th} and j^{th} atomic orbitals
H_0^o	Standard enthalpy at 0°K

ΔH_F^o	Standard heat of formation at 0°K
ΔH_s	Sublimation energy of graphite
k	Parameter in Eqs. 7 to 10 equal j/n; $j=1, 2, \ldots n-1$ in Eq. 7; $j=2, 3, \ldots n-1$ in Eq. 8; and $j=1, 2, \ldots n$ in Eqs. 9 and 10
k	Conductivity
$\widetilde{K}_i$	Mass fraction of ith chemical element
K_j	Mass fraction of jth chemical specie
K_p	Equilibrium constant at constant pressure
Le	Lewis-Semenov number $= \dfrac{\rho D \overline{C}_p}{k}$
M	Molecular weight, Mach number
m	Mass of carbon atom
$\dot{m}$	Mass flux
n	Number of carbon atoms
P	Pressure
$\dot{q}$	Heat transfer rate
r	Radial distance in ring molecule
R	Universal gas constant
R_{C_n}	Resonance energy of C_n species
s	Carbon-carbon distance
$\dot{s}$	Surface recession rate
S	Distance along body surface
S_{ij}	Overlap integral of ith and j^{th} atomic orbitals
T	Temperature
u, v	Components of velocity parallel and normal to surface
x	Moving coordinate
y	Fixed coordinate, distance measured from initial surface position, or boundary layer coordinate

Greek Symbols

ϵ	Emissivity, energy of molecular orbital
θ	Time
ρ	Density
σ	Stefan-Boltzmann constant
χ_B	Bending force constant
χ_S	Stretching force constant
χ_T	Torsional force constant
ω	Fundamental vibrational frequency

B	Binder, or bulk
C	Carbon
D	Diffusion controlled oxidation
e	Boundary-layer edge
F	Filler
g	Gases
i	Initial, or i^{th} element
j	j^{th} specie
L	Linear
R	Ring
s	Solid material, or sublimation
S	Stagnation
w	wall

I. Introduction

Carbon and its allotropic forms have been used extensively for thermal protection of super-orbital and strategic entry vehicles over the past decade. These materials are thermally attractive because of their ability to support high surface temperatures with comparatively low surface erosion. Although the carbonized and graphitic-carbon allotropes have been studied analytically with some vigor, recently developed high-pressure test facilities have revealed a large deficiency in analytical predictions of the observed mass-loss data. As a consequence, resort to empirical and semi-empirical correlations of the test data has resulted with rather drastic results evidenced in extrapolation to actual flight environments.

Understandably, empirical correlations of test data are at best provisional; little insight into the actual mechanisms operative during the ablation processes is gained[1, 2]. Conversely, rather sophisticated analyses of the thermochemical erosion of a variety of carbon-based materials has evolved[3, 4, 5]. Development of these analyses has been closely followed by a number of papers dealing with various aspects of the thermomechanical ablation problem[6, 7, 8], and are specialized to the particular material under study. The composite of these analyses has failed to provide repetitive correlation of the test data--obviating their generality. In retrospect, it appears that the physical model used to describe the ablation mechanisms has been neglected in deference to mathematical eloquence. It is now evident that a large number of disciplines are required to effectively approach the analytical description of even what previously was described as homogeneous materials; e.g., graphite.

This paper is directly concerned with the ablation performance of graphite in high-pressure environments. Here, the basic structure of bulk graphite is examined and used to formulate a model to describe the surface erosion mechanism. In the analysis development, attention is directed toward the heterogeneous structure of graphite, the formation of large polyatomic carbon-vapor species subliming from the heated surface, and the preferential erosion of dissimilar constituents within the graphite structure promoting removal of particulate solid. To achieve the analytical performance description, newly computed thermodynamic functions for the polyatomic ring and chain

carbon molecules are used to define the sublimation regime; the probable uncertainty in these functions on computed vapor pressure and mass transfer is evaluated. This uncertainty is carried throughout the paper to assess the sensitivity on computed surface recession and energy transfer in a self-consistent manner. Removal of graphite filler grains caused by preferential erosion of the binder matrix is formulated; numerical results are presented for the fraction of solid material eroded from the surface. To establish the solid fraction of eroded material, ablation test data in the 10- to 100-atm pressure range, encompassing fine- to coarse-grain filler particles, are correlated. The composite effect of thermochemical and thermomechanical erosion is depicted in the test data correlations. A priori, it should be understood that the proposed model is provisional in that the high-pressure test data lack the resolution necessary for detailed qualification of the analysis procedures (i.e., the individual grains are too small to be observed leaving the surface).

II. Bulk Graphite

There is an understandable tendency to treat graphite as a homogeneous solid when analyzing ablation processes; graphite consists of a single chemical element--carbon. Bulk graphite, by the nature of the process used in its formation, is far from homogeneous and failure to account for the heterogeneous structure leads to an incomplete description of the surface erosion mechanism. In this paper, bulk graphite denotes the different forms of carbon existing in the solid caused by differences in constituent materials forming the filler grains and binder matrix.

Physical Characteristics

An understanding of the microstructure of graphite requires some knowledge of the processes by which graphite is formed. The commercial graphites used in aerospace applications can be described as synthetic or manufactured. These bulk graphites are manufactured by mixing an organic binder, usually a coal tar pitch, with carbon filler particles and molding or extruding the mixture to form a "green" billet. The binder is then carbonized by heating to temperatures on the order of 1500°F, followed by further heating to temperatures up to 5400°F, to produce a more ordered microstructure. The filler material may be any particulate graphite or carbon, such as natural graphite, carbon black, coke, etc. For economic reasons, filler material is most commonly made from the coked residue of the petroleum refining process. The coke mass is crushed and ground to eliminate gross porosity, and screened into controlled particle sizes. Because of unavoidable intercrystalline micropores, the particles retain a minimum porosity of 5 to 8%[9], resulting in apparent densities of about 2.0 to 2.2 gm/cc.

Figure 1 provides a schematic of the proposed bulk graphite arrangement after graphitization*. The filler particles appear as an array of loosely packed irregular-shaped coke elements cemented together by the carbonized binder. The ratio of

---

*The description given here abets the excellent discussion of graphite by Riley[10].

2

binder-to-filler weight may be varied over wide limits, with normal practice being between 20 to 40%. In the baking cycle (1500°F) the pitch binder is pyrolyzed, losing about 40 to 50% of its initial weight. During the baking cycle, and upon subsequent graphitization, the binder shrinks. Since shrinkage is constrained by the filler particles, the volume nominally occupied by the binder has a large void content. The resulting macropores in the binder allow for easy passage of evolved gases through the binder matrix and account for the relatively high porosity of bulk graphite. Each filler particle is held in the resulting matrix by a network of binder bridges occasionally interrupted by interconnected macropores. The macropore diameter varies, but is about the same as the diameter of the filler particles. A line of interconnected macropores may propagate a mechanical failure since this is the path of minimum cross section. The microstructure evidenced in Figure 1 exposes the heterogeneous qualities of graphite in detail. Filler particles consist of closely packed crystallites and intercrystalline micropores. Significantly, the crystallites are not completely ordered; the binder crystallites are even less ordered; which accounts for the minimal anisotropy exhibited in the thermophysical properties of bulk graphite.
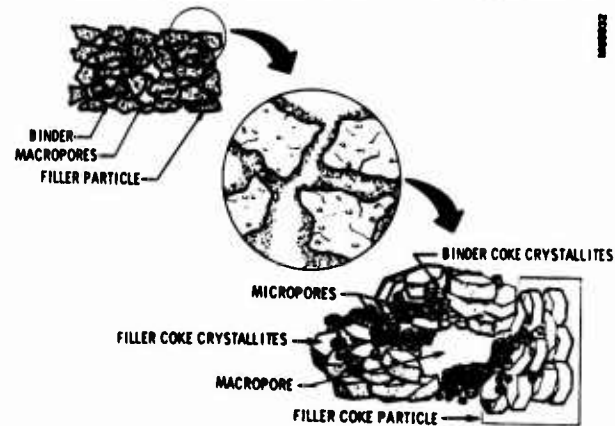

Figure 1. Schematic of Graphite Microstructure

In this paper ablation test data are presented for a number of commercial graphites encompassing fine- to coarse-grain filler particles. The mean particle diameters varied between 5 to 100 microns. A typical particle diameter distribution determined by a Coulter counter is shown in Figure 2. For this particular graphite, 50% of the particles evidenced a particle diameter greater than 4 microns. For the purpose of comparison, the diameter of a grain of sand is about 100 times larger. The heterogeneous character of graphite is again exhibited in the particle size distribution. Further, studies have been conducted, using X-ray diffraction analysis, on the effect of graphitization temperature on interlaminar spacing. Figure 3 shows distinctively different interlaminar spacings for the binder and filler. For this particular graphite, the filler particles appear to be completely graphitized at about 3000°C; the binder remains partially graphitized. Complete graphitization occurs when the lattice spacing is about 3.354A. Properties of the commercial graphites tested and presented here are given in Table I. Although the density range of the bulk graphites tested was not large, appreciable variations in constituent material content, density, and porosity are included. Nominal values cited are representative of the finer grain graphites.
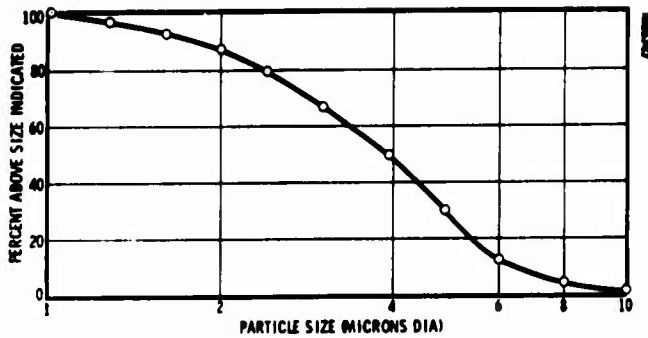

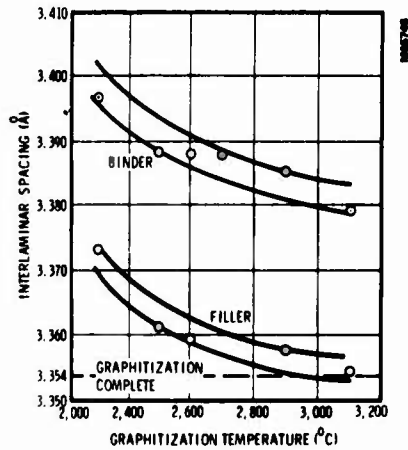Figure 2. Typical Particle Size Distribution

Figure 3. Interlaminar Spacing as a Function of Graphitization Temperature for Typical Fine-Grain Graphite

Table I

PROPERTIES OF BULK GRAPHITES

Property	Range		Nominal Value
ρ - Bulk density	1.65 to	1.95	1.8 gm/cc
ρ_F - Filler density	2.0 to	2.2	2.15 gm/cc
ρ_B - Binder bulk density	0.8 to	1.4	1.2 gm/cc
K_B - Mass fraction binder	0.2 to	0.4	0.25
ϵ_B - Binder porosity	30 to	50	40%

Analysis Model

Development of an analytical model to represent the complex and varied structure of graphite, as schematically portrayed in Figure 1, is not easily accomplished. Rather convincing evidence has been shown to destroy the concept of graphite as a homogeneous solid. It remains to construct a physical model whereby quantitative information concerning the surface erosion mechanism of the amorphous solid can be obtained.* To aid in formu-

---

*Presently, this analysis is limited to loss of particulate solid at the heated surface caused by preferential mass loss of the binder constituent; macrospallation (the loss of larger scale material) is omitted, as is very complex thermal stress failure.

3

lation of a performance model, many photomicrographs of graphites exposed to high-pressure jet heating conditions have been examined. Photomicrographs typical of the post-test condition of the sectioned test models (subsequently described) are given in Figure 4. The cross section for both a coarse- and fine-grain graphite is shown extending from the heated surface to the interior. Indicated in the figure is the irregular (roughened) surface consistent with the graphite microstructure shown in Figure 1. Pockets at the surface are evident (otherwise not seen in the pre-test models). Presumably, these are depressions caused by loss of particulate solid at the surface. Particularly noticeable is the open surface structure and increase in macropore area in close proximity to the surface. Attention should also be given to the rather random distribution of the pores and apparent interconnected pore structure.
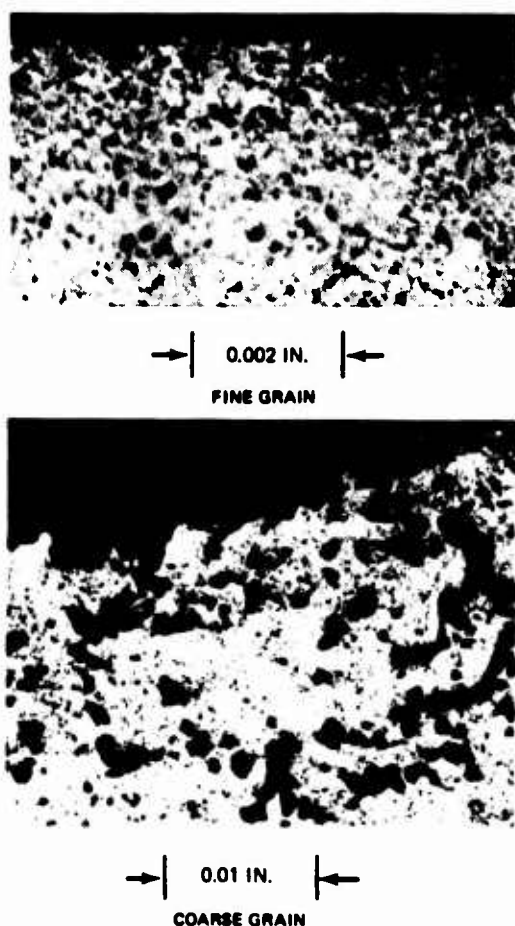

→| 0.002 IN. |←

FINE GRAIN

→| 0.01 IN. |←

COARSE GRAIN

Figure 4. Graphite Photomicrographs

The mechanism by which graphite surface erosion is effected can then be postulated. At elevated surface temperatures commensurate with the high pressures addressed here, molecular oxygen reacts chemically with the surface, independent of the orientation of the crystallites (hence, exposure of edge planes). The extent of oxidation is determined solely by the transport rate of oxygen to the surface, and is thus diffusion controlled. The order of the crystallites, however, is reflected to an extent on the solid properties; entropy directly reflects the disorder. At surface temperatures in excess of 5000°R (the threshold temperature for sublimation) considerable quantities of carbon vapor are evolved from the solid. Sublimation is not constrained to the surface; the open, 3-dimensionally

connected binder structure beneath the surface affords a means by which internal sublimation can occur. Preferential erosion of the binder constituent is primarily by these two mechanisms, exposing filler particles at the heated surface.

The phenomenon causing loss of particulate solid at the surface is shown schematically in Figure 5. Filler particles of mean characteristic dimension, $\bar{h}$, are exposed above the receding surface at an initial height, h. During this time increment, the particle recedes by an amount, S_F, caused from chemical consumption via chemical reactions with boundary layer air reactants and by direct sublimation. A transformed coordinate system (y fixed in space) is utilized to describe particle exposure in terms of particle and binder recession rates. The individual recession rates for the binder and filler phases are, respectively,

$$\dot{S}_B = \dot{m}_B / \rho_B \qquad (1)$$

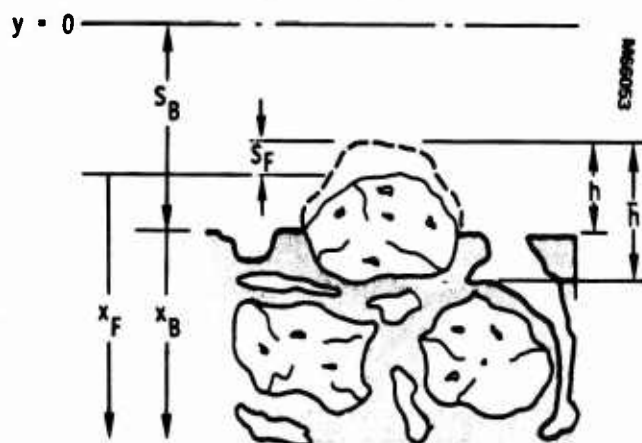$$\dot{S}_F = \dot{m}_F / \rho_F \qquad (2)$$

Figure 5. Particle Erosion

Employing the transformed coordinate system, the actual height of the exposed filler particle above the moving coordinate, x_B, is

$$\frac{x_F - x_B}{\bar{h}} = \left(1 - \frac{\dot{m}_F}{\dot{m}_B} \cdot \frac{\rho_B}{\rho_F}\right) \frac{h}{\bar{h}} \qquad (3)$$

Equation 3 provides definite information about particle exposure. At this time, the ratio of mass fluxes in Equation 3 is taken as unity, assuming identical properties of the two solid phases as affects mass transfer. Referring to Table I the density ratio is about 0.5. Thus, for a particle not acted upon dynamically, and fully exposed (h/$\bar{h}$ = 1), the particle has receded half-way through the exposed height and is freed from the binder. In the dynamic situation, exposure of particles occurs continuously, and subsurface sublimation causes loss of binder, burning through the binder bridges holding the particles as the macropores enlarge. During this time the particles exposed have partially receded. Finally, the filler particles are restrained only by geometric interlocking with adjacent particles, and presumably, would be blown free by moderate pressure or shear forces. The erosion of individual filler particles is consistent with available ablation data, since the particles are too

4

small (0.02 to 5 microns) to be observed by normal photographic techniques, and the surface would appear to ablate uniformly. Preferential loss of binder and expulsion of filler particles from the surface has been observed by Wachi[11] in free vaporization studies conducted on a number of graphite test samples.

The remainder of this paper is devoted to determination of the fraction of particulate solid eroded from the receding surface in terms of environmental exposure conditions. To accomplish identification of the thermomechanical recession component from surface erosion measurements of the test data we first describe the thermochemical recession in some detail. The probable uncertainty in thermodynamic data employed on surface recession rates is evaluated in a description of sublimation rates. Loss of particulate solid at the heated surface is then addressed as affects mass and energy transfer. Correlation of the experimental data in terms of thermochemical erosion enables quantitative identification of the solid fraction eroded.

III. Carbon Thermodynamics

Considerable interest and research have been focused on the identification and thermodynamic characterization of high-temperature carbon vapor species, and elucidation of the carbon vapor equation of state. Up to now, the thermodynamic properties of all polyatomic carbon vapor species larger than C_3 have been calculated[12, 13, 14] from the (L-F) " " increments of Pitzer and Clementi[12], which were fitted to yield a triple-point pressure of 100 atm at $4000°K$[15]. Likewise, the equation-of-state calculations[13, 14, 16, 17, 18] have failed to include the heavier molecular weight species C_{17} to C_{30}, despite evidence of their existence[19, 20] and likelihood of their prominence at high pressures and temperatures. The carbon ring molecules have also been excluded. In this paper, both linear and polygonal ring structures of C_n are considered up to C_{30}. The resonance energies and, ultimately, the thermodynamic properties of the molecules are calculated by theoretical methods substantially different from those used by Pitzer and Clementi[12] and later by Strickler and Pitzer[21]. The theoretical procedures are internally self-consistent, and yield results which are in good agreement with the observed sublimation data and recent triple-point temperature measurements of graphite.

Vapor Properties

The molecules studies were linear chains with 4 to 30 carbon atoms, and regular polygonal rings with 3 to 30 carbon atoms. Figure 6 depicts the assumed valence bond configuration for each type of structure. Bonding is assumed to consist of localized σ bonds and delocalized π bonds constructed from linear combinations of 2_{p_π} atomic orbitals. The carbon-carbon distance is taken as 1.28A: the bond length in C_3[22] and the C=C distance in carbon suboxide, C_3O_2[23]. The π orbitals in the linear chains are delocalized with respect to the xz and yz planes, with the 2_{p_π} atomic orbitals pointing in the x and y directions. The ring compounds have a set of π orbitals formed from 2_{p_π} atomic orbitals oriented perpendicular to the plane of the ring and another set formed from 2_{p_π} orbitals oriented radially in the plane of the ring. Except in large

rings, the latter do not exhibit true π-bond behavior because of increasing s and p orbital interaction with increased bending of the carbon-carbon chain. The electronic ground state of linear C_n is $\sum_g^+$ if n is odd, and $\sum_g^-$ if n is even. In the ring molecules, the singlet state occurs where n is even, and the triplet state where n is odd.
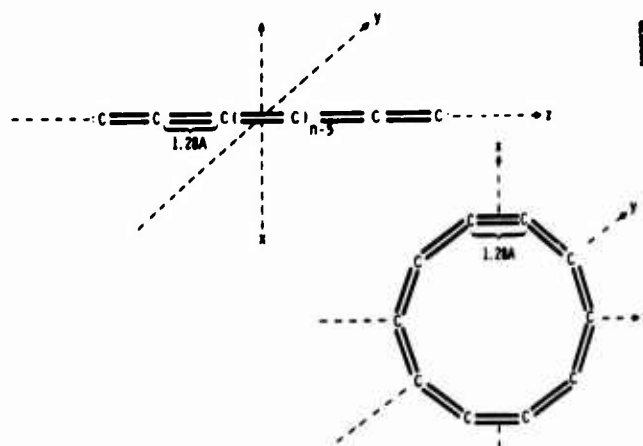

Figure 6. Valence Bond Structure for C_n Linear Chain and C_{10} Polygonal Ring

The heats of formation of the polyatomic carbon species were calculated from the relations of Strickler and Pitzer[21].

Linear Molecules

$$\Delta H^o_{C_n}(L) = \Delta H^o_{C_3}(L) + R_{C_n}(L) - R_{C_3}(R)$$

$$+ (n-3)E_i - 23/n\ \{1 - Mod(n, 2)\}\quad (4)$$

Ring Molecules

$$\Delta H^o_{C_n}(R) = nE_i + R_{C_n}(R) - 23/n\ Mod(n, 2)\quad (5)$$

The operator Mod (n, 2) in Equations 1 and 2 is defined as $n - 2\ \{n/2\}$ and is a correction for the difference in energy between the triplet electronic ground state and the slightly higher singlet state associated with the calculation.

E_i (the energy per interior carbon atom) was set equal to 43.4 kcal/mole, the value calculated by Pitzer and Clementi[12] from the energy difference in allene-ethylene, corrected by the (L-F) method for the effect of hyperconjugation. $\Delta H^o_{C_3}(L)$ was computed to be 202.6 kcal/mole from Drowart's[24] mass spectrometric data, the Third Law relationship, and the thermodynamic properties of linear C_3 calculated here. A good method is not available for estimating the energy of the terminal atoms in a linear chain; the observed value of $\Delta H^o_{C_3}(L)$ is taken as the reference point.

The resonance energy, R, of an unsaturated molecule is defined as the difference in electronic energy of the actual delocalized structure and a hypothetical localized double-bond configuration.

The energies of the delocalized and localized molecular orbitals were calculated by the extended Hückel technique of Hoffmann[25]. In particular, the delocalized energy was obtained by solving the complete set of Hückel equations

$$\sum_{i=1}^{n} \left[H_{ij} - \epsilon S_{ij} \right] C_i = 0 \qquad j = 1, 2, \ldots n \qquad (6)$$

using as a basis set n 2s and 3n 2p carbon Slater orbitals with exponents of 1.625. The matrix elements, H_{ij}, were evaluated by the relations in Reference 25, the overlap integrals, S_{ij}, were calculated directly. The energy for the hypothetical localized structure was obtained from Equation 6 by setting some of the H_{ij} and S_{ij} matrix elements of the $2p_\pi$ atomic orbitals equal to zero, so as to have a localized structure.

Because of the extremely large computer run times required for the larger species (e.g., 1.3 hours for C_{24}), the resonance energies of the large molecules were obtained by the interpolation or extrapolation of smooth curves constructed from the calculated resonance energy data of linear and ring C_3 to C_{18} and C_{24}. Small errors introduced by this procedure are of no consequence except, perhaps, at very high temperatures and pressures outside the range of this study. The delocalized energies of several of the carbon species were taken directly from Hoffmann's orbital energy data[26]. These energies were obtained for a C–C distance of 1.30A for the C_n species; however, the use of 1.30A instead of 1.28Å has no significant effect on the calculated energy. Table II lists the resulting heats of formation of both the linear and ring carbon vapor species; the values of ΔH_F^0 for C_1 and C_2 were obtained from Reference 24. The calculated heats of formation for cyclic C_3 and C_4 were found to be too low due, presumably, to an underevaluation of the strain energy. These molecules are not included in these calculations. In addition, another set of ΔH_F^0 values was calculated using the method of Strickler and Pitzer[21]. (A revised version of the original Pitzer and Clementi calculation.) These alternate calculations were performed with a strain energy for the ring compounds of 154.5/n kcal/mole based on a fundamental bending frequency of 63 cm^{-1} for C_3O_2, and a heat of formation of 202.6 kcal/mole for linear C_3. The ΔH_F^0's obtained by the Hoffman method[25] were as much as 150% larger for cyclic C_6, and an average of 16% and 18% larger for cyclic and linear C_{20} to C_{30}, than the values obtained by Strickler and Pitzer. These differences may be partially accounted for by the different definitions of H_{ij} utilized in the two methods. However, the extended Hückel theory of Hoffman, unlike the LCAO-MO method of Strickler and Pitzer, treats the entire secular determinant (including non-nearest neighbor interactions), and takes into account the precise atomic coordinates of the various atoms. Other considerations being equal, the above should result in orbital energies which are more accurate. This is particularly true in the case of the intermediate-size ring species.

Thermodynamic properties of the carbon vapor species were calculated by the well-known relations of statistical mechanics. The electronic states of C_1 were obtained from Reference 27. The spectroscopic constants of C_2 were taken from References

28 and 29. The constants for C_3 were obtained from Reference 30; a bending force constant of 63 cm^{-1} [31] was employed in the calculation. The spectroscopic constants (i.e., moments of inertia and fundamental vibrational frequencies) of all other carbon vapor species were calculated and derived directly. Equations for calculating the fundamental vibrational frequencies of the linear and ring molecules were derived from a normal coordinate analysis of the molecule. Assumptions were made in the derivation that the valence force-field consisted of bending, stretching, and (in the case of rings) torsional motion; and that all motions were harmonic in nature, and mutually independent. The equations for the fundamental frequencies, (cm^{-1}), associated with each type of structure and molecular motion are given below:

Linear Molecule

(a) Stretching motion

$$(2\pi c\omega)^2 = (4X_S/m) \sin^2 (k/2) \qquad (7)$$

(b) Bending motion

$$(2\pi c\omega)^2 = (16X_B/m) \sin^4 (k/2) \qquad (8)$$

$$(2\pi c\omega)^2 = 1/2 \left(f_{11} + f_{22} \pm \sqrt{(f_{11} - f_{22})^2 + 4f_{12}^2} \right) \qquad (9)$$

$$f_{11} = (8X_S/m)(r/s)^2 \sin^4 (\pi/n)(1 + \cos k)^2$$
$$+ (2X_B/m)(r/s)^2 \sin^2 (2\pi/n)(3 + \cos 2k - 4\cos k)$$

$$f_{22} = (8X_S/m)(r/s)^2 \sin^2 (\pi/n) \cos^2 (\pi/n)(1 - \cos k)$$
$$+ (2X_B/m)(r/s)^2 (2 \sin^2 \pi/n)^2 (1 - \cos 2k)$$

$$f_{12} = (8X_S/m)(r/s)^2 \sin^3 (\pi/n) \cos (\pi/n) \sin k$$
$$+ (2X_B/m)(r/s)^2 \sin (2\pi/n)(2 \sin^2 \pi/n)^2$$

$$(\sin 2k - \sin k) \quad (2\pi c\omega)^2 = (8X_T/ms^2 \sin^2 2\pi/n)$$

$$\times (1 - \cos k)(\cos k - \cos 2\pi/n)^2 \qquad (10)$$

X_S, X_B and X_T are the respective stretching, bending and torsional force constants for both chain and ring structures. The bending mode frequencies in Equation 8 are doubly degenerate, and Equations 9 and 10 are zero for three distinct values of j. Consequently, Equations 7 through 10 yield a total of 2n-5 and 2n-6 values (not necessarily distinct) of ω in the case of the linear and ring molecules, respectively, in accordance with the principle of equipartition. The force constants x_S and x_B were assigned the values 11.83 x 10^5 dyne cm^{-1} and 5,100 dyne cm^{-1}. These are the magnitudes of the carbon-carbon stretching force constant[32] and the central carbon bending force constant[33] of C_3O_2. X_T was set equal to 3.36 x 10^{-12} erg/rad, the value of the torsional force constant of benzene[34].

Table II
PROPERTIES OF CARBON SPECIES

Molecule	Linear Structure (KCAL/MOLE)				Ring Structure (KCAL/MOLE)			
	ΔH^o_f	ΔF^o_f			ΔH^o_f	ΔF^o_f		
	0°K	2000°K	3000°K	4000°K	0°K	2000°K	3000°K	4000°K
C_1	169.6	95.9	58.6	21.5				
C_2	197.0	106.8	62.2	18.7				
C_3	202.6	95.2	42.3	-9.5				
C_4	248.1	131.6	74.2	18.1				
C_5	255.6	133.4	72.7	13.3	327.4	218.2	167.0	117.5
C_6	303.6	161.2	90.0	20.2	268.6	161.2	111.1	62.8
C_7	317.5	169.0	94.3	21.1	320.7	201.0	144.8	90.7
C_8	362.0	193.0	107.7	23.9	324.1	206.2	151.3	98.5
C_9	383.3	208.0	119.0	31.7	328.0	197.7	137.0	78.5
C_{10}	423.3	227.3	127.6	29.6	295.7	167.3	107.9	50.8
C_{11}	454.1	251.6	148.2	46.6	363.3	222.5	157.4	94.8
C_{12}	484.6	261.3	147.1	34.8	390.8	251.8	188.2	127.2
C_{13}	505.6	275.7	157.8	41.8	409.4	258.0	188.9	122.4
C_{14}	546.7	296.0	167.1	40.3	395.1	245.5	178.0	113.3
C_{15}	572.1	314.7	182.0	51.5	458.4	296.4	223.4	153.5
C_{16}	611.7	333.3	189.8	48.4	486.4	326.3	254.9	186.9
C_{17}	642.5	357.4	210.0	64.9	511.4	338.8	262.1	188.9
C_{18}	676.6	370.5	212.2	56.2	498.2	327.5	252.5	181.3
C_{19}	705.3	392.4	230.2	70.5	564.4	381.2	301.0	224.8
C_{20}	739.5	405.5	232.4	61.8	595.0	413.7	335.3	261.1
C_{21}	774.1	433.3	256.3	81.9	625.3	431.5	347.9	268.8
C_{22}	807.0	445.1	257.1	71.8	622.8	430.9	349.2	272.3
C_{23}	841.9	473.1	281.3	92.2	691.7	487.3	400.5	318.7
C_{24}	876.0	486.1	283.3	85.2	728.2	525.7	440.8	361.3
C_{25}	911.2	514.4	307.7	103.8	761.4	546.5	456.4	372.2
C_{26}	944.7	526.7	309.0	94.2	767.4	554.3	466.3	384.4
C_{27}	981.5	556.6	335.0	116.4	839.4	613.9	520.8	434.2
C_{28}	1016.1	569.0	337.4	107.8	879.2	655.5	564.5	480.3
C_{29}	1054.3	601.3	364.7	131.3	918.2	682.7	586.7	497.8
C_{30}	1086.9	612.7	365.1	120.8	928.0	802.4	599.8	513.4

Solid-Vapor Equilibrium

Table II lists the standard-state free energies of formation of the individual carbon species at three different temperatures, calculated from

$$\Delta F^o_F = \left[\Delta H^o_F + F^o - H^o_o \right]_{C_n} - n \left[F^o - H^o_o \right]_{C_s} \quad (11)$$

related to the partial pressure, P_{C_n}, of C_n by the equilibrium constant

$$- \frac{\Delta F^o_F}{RT} = \ln K_p \quad (12)$$

and

$$K_p = P_{C_n} \quad (13)$$

The free energy of graphite solid used in Equation 11 was taken from JANAF[30].

Figures 7 and 8 depict the logarithms of the partial pressures of the respective linear and ring molecules in equilibrium with graphite. The plots show linear C_3 is the most stable species and linear C_5 somewhat more stable than C_4 and C_6, in agreement with previous mass spectrometric findings[19,24]. It is also apparent that the contribution of ring molecules is negligible, and that larger linear molecules become very important at 4500°K,

and should be included in calculations performed above 4000°K. Except for C_3, and possible C_5, the odd-even alternation in stability computed by Pitzer and Clementi, and observed by Baun and Fischer up to C_9, is not found in the linear chain data of Figure 7. However, the measurements of Baun and Fischer were made on ions, and the trend in stability may shift when applied to the neutral counterparts. These investigators obtained increased concentrations of doubly charged ions C_n^{2+} with n = 11, 15, 19 (whose structures are believed to resemble the closed-shell configurations of the neutral cyclic species C_{10}, C_{14}, C_{18}) which have superior stabilities (as shown in Figure 8). In Figure 7, an even-odd alternation is evident above C_{10} at 4000°K; the effect appears to propagate to smaller values of n with increasing temperature.
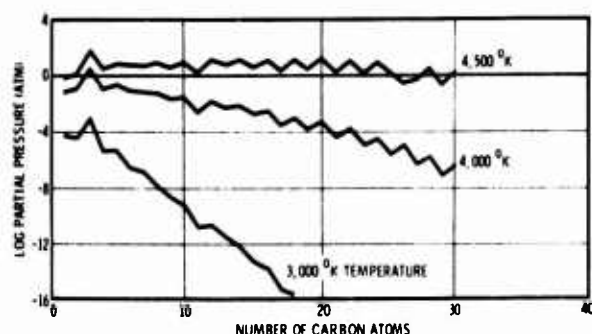

Figure 7. Partial Pressures of Linear Carbon Vapor Species
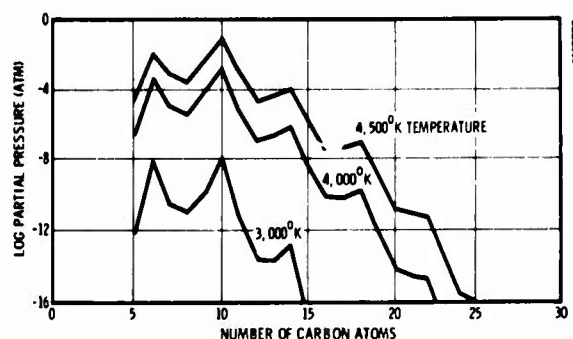

Figure 8. Partial Pressures of Ring Carbon Vapor Species

In Figure 9, the total pressure of the vapor in equilibrium with graphite

$$P = \sum_{n=1}^{30} \left[P_{C_n}(L) + P_{C_n}(R) \right] \quad (14)$$

is shown and compared to that calculated by Pitzer and Clementi, and Duff and Bauer. It is apparent the data of Pitzer and Duff do not agree well with the experimentally determined sublimation point of Thorn and Winslow[35] and the recent triple-point temperatures of Schoessow[36] and Fateeva[37]. The results obtained match the sublimation point and lie between the more recent triple-point temperatures. This calculation method is advantageous because (1) it generates the thermodynamic properties of both linear and ring structures in a self-consistent manner, and (2) the resulting data, used in conjunction with the new heat of formation values, are consistent with the latest experimental data without recourse to alteration.
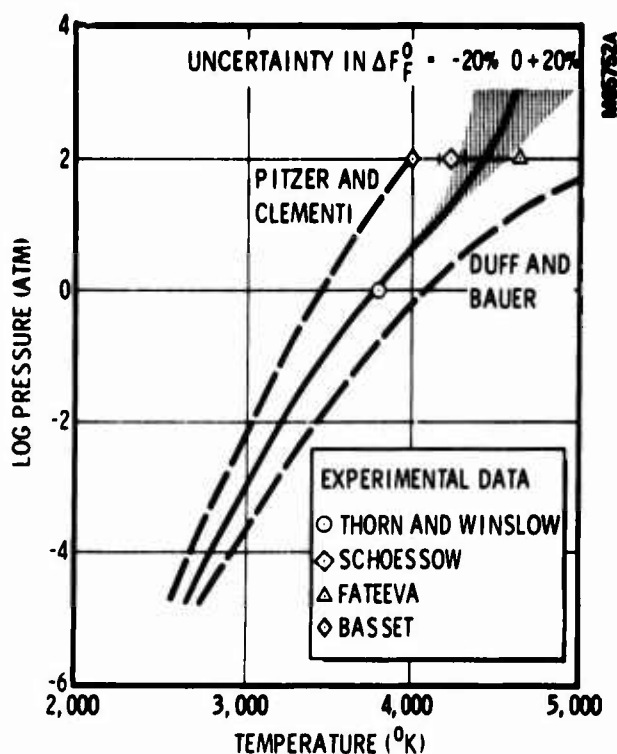
7

Figure 9. Graphite Equilibrium Vapor Pressure

total equilibrium pressure (Figure 9) (hence the number of moles of each species) increases substantially as the free energy of formation is decreased. The effect on the average molecular weight and sublimation energy is likewise pronounced. The trend in Figure 12 is for larger values of $\bar{M}$ with decreasing ΔF_F^0. This is due to the larger increase in population of the heavier molecular weight species in relation to the lighter species. In Figure 13, the sublimation energy of graphite, which is defined as

$$\Delta H_s = \sum_{n=1}^{30} \frac{P_{C_n}(L)}{P} H_{C_n}(L)$$

$$+ \frac{P_{C_n}(R)}{P} H_{C_n}(R) - H_{C_s} \qquad (15)$$

tends to decrease significantly as the free energy of formation is increased.

Because the free energies of formation ultimately control the state properties of the system, the influence of ΔF_F^0 on the state properties was studied. Calculation of these properties was repeated with the free energy of each species with $n > 3$ perturbed by $\pm 20\%$. The limits were adopted on consideration of the probable cumulative uncertainty in the calculated heats of formation and free energy[*]. The uncertainty limits reflect a study of the influence of key spectral quantities and methods on these properties. As discussed previously, our heats of formation for the large molecules are about 18% greater than the Strickler and Pitzer values, accordingly increasing ΔF_F^0. In calculation of the free energy, an evaluation was made of the effect of the bending force constant (X_B) in perturbing the results. The bending force constant contributes more strongly to the thermodynamic properties than the stretching and torsional force constants. Figures 10 and 11 show the influence of X_B on the free energy for selected linear and cyclic molecules. The free energy and hence the free energy of formation decrease markedly as the bending force constant is decreased below 5,100 dyne cm^{-1}. A 50% decrease in X_B, for example, lowers the free energy of formation approximately 10% at 3000°K and 20% at 4000°K for the larger species. Thermodynamic calculations made here used the bending force constant for C_3O_2 (5,100 dyne cm^{-1}). This molecule was selected because of the similarity in bonding with C_n and because the carbon atoms are less apt to exhibit terminal end effects than the atoms in C_3.

Figures 9, 12 and 13 show the effect of the uncertainty in ΔF_F^0 on the respective equilibrium vapor pressure, average molecular weight of the vapor, and sublimation energy of graphite. The
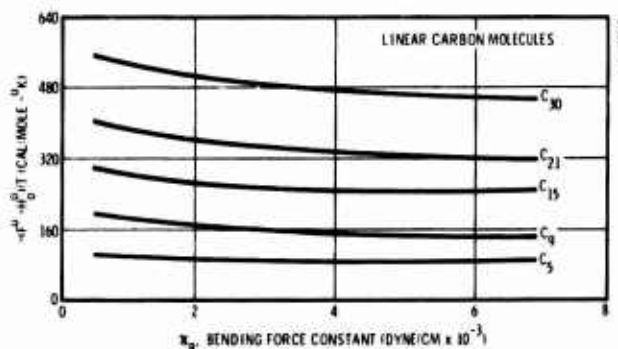

Figure 10. Influence of Bending Force Constant on Free Energy at 3,000°K

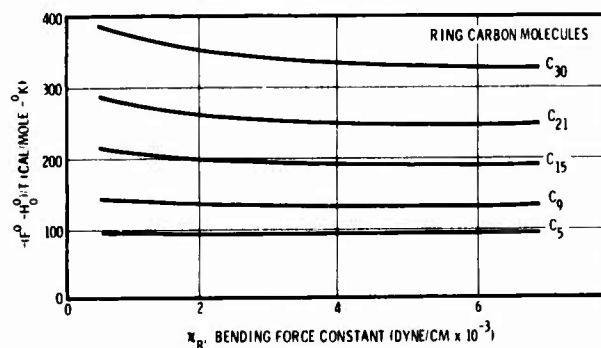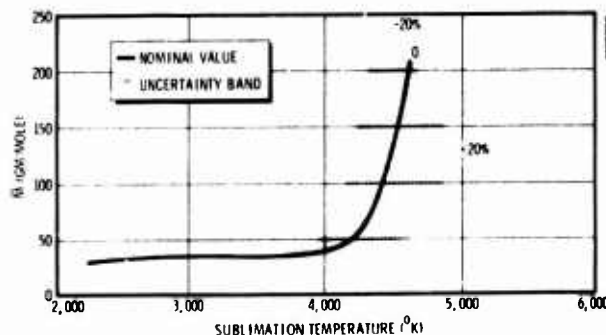**Figure 11. Influence of Bending Force Constant on Free Energy at 3,000°K**

Figure 12. Carbon Vapor Molecular Weight

[*] The much smaller uncertainty in the properties for C_1-C_3 is omitted in these calculations.
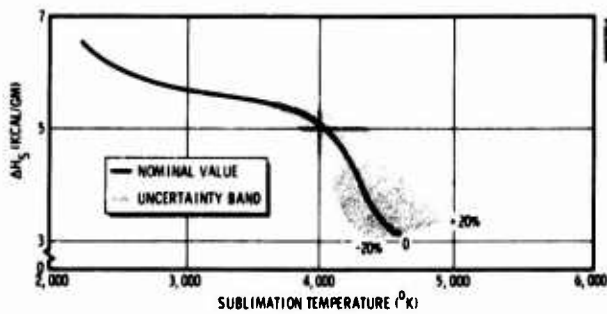
8

Figure 13. Graphite Sublimation Energy

IV. Mass and Energy Transfer

Application of the governing conservation equations to an ablating body with internal gas generation has been well studied. Basically, the differential equations used to describe thermo-chemical erosion in multicomponent-chemical reacting flows, stem from the hypersonic approximations of Lees[38], formulations of Scala[3], and those derived by Dorrance[39]. When similarity constraints are retained (e.g., at the stagnation point, and for certain body geometries) the differential equations reduce to differences only in the thermodynamic and transport properties employed and the numerical techniques used. Lees adopts the effective binary diffusion coefficient model with unity Lewis-Semenov number, obtaining a direct solution for mass and energy transfer. Scala obtains numerical solutions to the differential equations employing transport and thermodynamic properties for each chemical species included in his reaction system, which appears limited by present-day computer storage capacity. An approximation to large multicomponent reaction systems has been developed by Kendall, et al.[40] utilizing the differential equations of Dorrance, and achieving more versatility than either Lees or Scala. It remains that significant differences between the several sets of solutions, when using identical thermodynamic properties, has yet to be demonstrated.* Thus, the numerical results calculated here retain the similarity approximations of Lees.

Mass Transfer

The elemental mass balance of a material consisting of i-chemical elements whose surface recedes at a rate $\dot{s}$ and undergoing loss of solid material, $\dot{m}*$, at the surface (Figure 14) is given by

$$\dot{m}_g \tilde{K}_{i_g} + \dot{m}_s \tilde{K}_{i_s} - \dot{m}* \tilde{K}_i* - (\rho v)_{i_w} = 0 \quad (16)$$

where $\dot{m}_g \tilde{K}_{i_g}$ and $\dot{m}_s \tilde{K}_{i_s}$ are the mass fluxes of the element i into a control volume fixed at the receding surface owing to an internal gas source and solid material transfer, respectively. Mass leaves the control volume normal to the wall by a net flux of gas, $(\rho v)_{i_w}$, and by loss of solid, $\dot{m}* \tilde{K}_i*$. The mass flux of the ith element normal to the wall accrues by a summation of individual flux components consisting of the internal gas source, surface chemical reactions with the

---

*Comparisons between the equal and unequal diffusion coefficient model of Lees and Scala has been made by Hearne, et al.[41] and Dolton, et al.[14].

external reactive gas (boundary layer and internal gas species) and by direct sublimation. For graphite in an air boundary layer the following conservation statements are made at the wall, (c.f., Lees, Kratsch, et al.[5]).
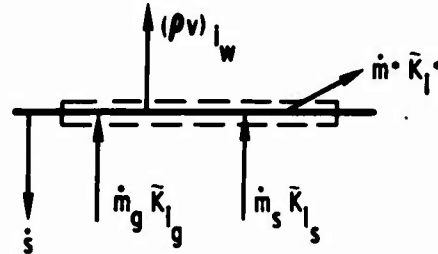

Figure 14. Mass Transfer

$$\tilde{K}_{N_w} + \tilde{K}_{O_w} + \tilde{K}_{C_w} = 1 \quad (17)$$

$$(\rho v)_{C_w} = \rho v_w = \rho v_w \tilde{K}_{C_w} - \left(\frac{\rho D \partial \tilde{K}_C}{\partial y}\right)_w \quad (18)$$

$$(\rho v)_{O_w} = 0 = \rho v_w \tilde{K}_{O_w} - \left(\frac{\rho D \partial \tilde{K}_O}{\partial y}\right)_w \quad (19)$$

$$(\rho v)_{N_w} = 0 = \rho v_w \tilde{K}_{N_w} - \left(\frac{\rho D \partial \tilde{K}_N}{\partial y}\right)_w \quad (20)$$

The gradient of the individual chemical elements at the wall is given by, e.g., carbon

$$\left(\frac{\partial \tilde{K}_C}{\partial y}\right)_w = \left(\frac{\tilde{K}_{C_e} - \tilde{K}_{C_w}}{H_{S_e} - H_w}\right)\left(\frac{\partial H}{\partial y}\right)_w \quad (21)$$

and for unity Lewis-Semenov number the convective heat transfer to the wall by conduction and diffusion is, upon introduction of Stanton number

$$\dot{q}_{conv} = \left(\frac{k}{\bar{C}_p} \frac{\partial H}{\partial y}\right)_w = \rho_e u_e C_H \left(H_{S_e} - H_w\right) \quad (22)$$

Thus, Equation 16 can be solved by introducing Equations 18, 21, and 22 and, after rearrangement, the elemental mass fraction of carbon at the wall is given by

$$\tilde{K}_{C_w} = \frac{\tilde{K}_{C_e} + \dfrac{\dot{m}_g \tilde{K}_{C_g}}{\rho_e u_e C_H} + \dfrac{\dot{m}_s \tilde{K}_{C_s}}{\rho_e u_e C_H} - \dfrac{\dot{m}* \tilde{K}_C*}{\rho_e u_e C_H}}{1 + \dfrac{(\rho v)_w}{\rho_e u_e C_H}} \quad (23)$$

9

where for graphite in an air boundary layer

$$\rho v_w = \dot{m}_g + \dot{m}_s - \dot{m}^*$$

$$\begin{aligned}
\tilde{K}_{C_e} &= 0 & \tilde{K}_{C_g} &= 1 \\
\tilde{K}_{N_e} &= 0.768 & \tilde{K}_{C_s} &= 1 \\
\tilde{K}_{O_e} &= 0.232 & \tilde{K}_{C}^* &= 1
\end{aligned} \qquad (24)$$

The fraction of solid entering the control volume which is lost at the surface as particulate solid is defined from Equation 24

$$\rho v_w = \dot{m}_g + \left(1-f_s\right)\dot{m}_s$$

$$\dot{m}^* = f_s \dot{m}_s \qquad (25)$$

Inspection of Equation 23 shows that the mass fraction of the element carbon at the wall is determined solely by the mass flux of elemental carbon injected at the surface as vapor, reflected by the difference in fluxes entering and leaving the control volume. Equations similar to Equation 23 for the element oxygen and nitrogen provide the necessary relations satisfying Equation 17 in terms of the individual fluxes depicted in Figure 14. A stoichiometric statement then directly relates the elemental mass fractions to the chemical composition of the combustion-sublimation species at the ablating surface

$$\tilde{K}_i = \sum_j \frac{\nu_i M_i}{M_j} K_j \qquad (26)$$

Numerical solutions to the governing equations were made invoking the chemical equilibrium constraint. The chemical reaction system included sublimation species for the ring and chain molecules given in Table II, and in addition air species, and carbon-air reaction products listed below*

O	NO	CO_2
O_2	N_2O	CN
N	NO_2	C_2N_2
N_2	CO	C_4N_2

Graphite sublimation rates over a large pressure range are shown in Figure 15 normalized to the familiar diffusion-controlled oxidation rate ($\dot{m}_D = 0.174 \, \rho_e u_e \, C_H$). In the first several decades of pressure the threshold sublimation temperature increases with increasing pressure reflecting the carbon-vapor-pressure diagram shown in Figure 9. The 10^1 to 10^3 atm pressure range is of special interest; the threshold sublimation temperature is compressed due to sublimation of large quantities of polyatomic carbon-vapor species. Thus, the high-pressure sublimation regime of graphite occurs over a fairly narrow surface temperature range (circa 7,000-8,000°R)in contrast to Scala's[3] results(7,000-10,000°R)which

---

*Thermodynamic property data for these species were taken from the JANAF tables.

omit carbon molecules larger than C_3. Upon definition of a surface-energy balance and the in-depth heat conduction, sublimation rates are directly coupled to surface temperature and pressure and the local aerodynamic heating.
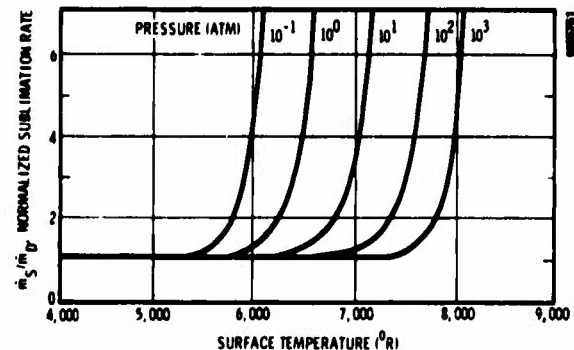

Figure 15. Graphite Sublimation Rate

Energy Transfer

Energy transfer to a surface undergoing material consumption via thermochemical erosion and thermomechanical loss of solid is given by an energy balance, Figure 16. The heat conducted by the solid away from the surface reflects the energy fluxes leaving and entering the control volume expressed in the following:

$$\dot{q}_{conv} + \underset{in}{\dot{q}_{rad}} - \underset{out}{\dot{q}_{rad}} - (\rho v)_w \, H_w - \dot{m}^* H_s =$$

$$\dot{q}_{cond} - \dot{m}_g H_g - \dot{m}_s H_s \qquad (27)$$

where

$$H_w = \sum_j K_j H_j$$

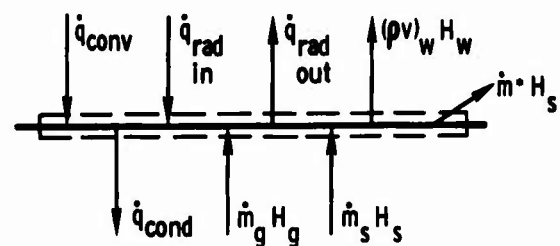$$H_j = \int C_p dT + \Delta H_F^o \qquad (28)$$

Figure 16. Energy Transfer

The summation in Equation 28 is made over all species in the gas at the wall with concentrations defined by the mass-transfer rates and application of the equilibrium constant. For the case of Le = 1 the net heat transfer to the surface may be expressed as (at this time $\dot{m}_g$ is set equal to zero)

$$\dot{q}_{cond} = \rho_e u_e \, C_H \left[H_{S_e} + \left(1-f_s\right) B_s' H_s - \left(1+B_w'\right) H_w \right]$$

$$+ \underset{in}{\dot{q}_{rad}} - \epsilon \sigma T_w^4 \qquad (29)$$

10

when the usual definition of the mass transfer parameter is made

$$B' = \frac{\dot{m}}{\rho_e u_e C_H} \qquad (30)$$

The reduction in Stanton number due to mass injection is functionally dependent on blowing rate, condition of the boundary layer, and properties of the injected species

$$\frac{C_H}{C_{H_o}} = f\left(\rho v_w , M_{inj}\right) \qquad (31)$$

Equation 29, when coupled to a standard finite difference solution to the conduction equation enables a complete description of the surface erosion of graphite including solid loss. It is observed that the effect of solid removal on the surface energy balance is to reduce the net energy transfer. For example, at a surface temperature of 7,500°R the $B'_s H_s$ term is about 1,700 Btu/lb at 100 atm pressure; Equation 29 is reduced only by 850 Btu/lb for $f_s = 0.5$. In comparison, the enthalpy of the combustion-sublimation products at the ablating surface is about 4,000 Btu/lb as shown in Figure 17. The enthalpy of the gaseous products (given by Equation 28) evidences the exothermic CO chemical reaction product below 5,000°R surface temperature. The increase in enthalpy above 5,000°R is coincident with sublimation; highly endothermic carbon vapor species evolve at the surface.
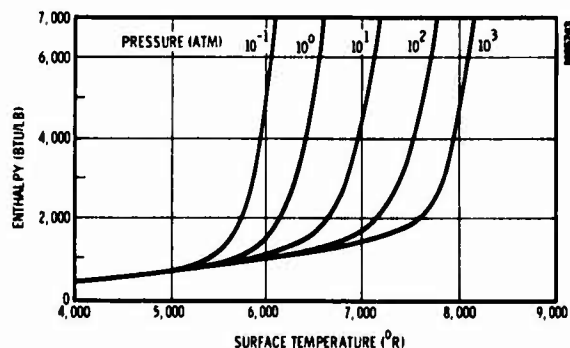
Figure 17. Enthalpy of Combustion-Sublimation Products at Ablating Graphite Surface

Detailed results of the high-pressure sublimation regime are shown in Figure 18. The chemical composition at the ablating graphite surface is given at 100 atm pressure. In addition to the air-carbon reaction products, a complex set of sublimation species is evidenced. The triatomic carbon-molecule is most abundent; however, a large number of polyatomic molecules of rather low concentration are seen. Other than C_3 the prevalence of any single carbon vapor species is not evident. Although vapor species having ring structures were included in the numerical computations, the concentrations shown are due only to linear structured molecules. Conclusively, the ring molecules can be safely neglected in performance analyses for graphitic materials. Omission of the linear carbon species at high pressures examined here may be quite critical as affects mass transfer.
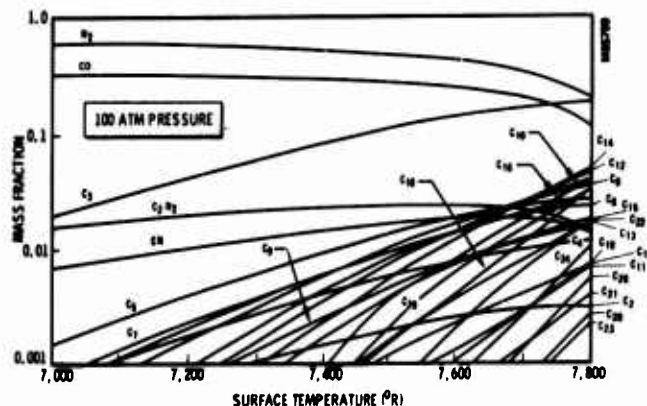
Figure 18. Chemical Composition at Graphite Surface

It is interesting to examine how the ablated mass of carbon is partitioned among the chemical composition shown in Figure 18. In Figure 19 the elemental mass fraction of carbon is shown extending from the diffusion-controlled oxidation regime well into the sublimation regime. As indicated, the constant mass fraction of 0.15 reflects the carbon mass in CO. At about 6,500°R nitrogen reacts forming the cyano radical and cyanogen; only a small mass of carbon is ablated because of these reaction products. At about the same temperature (6,500°R) contributions due to C_1 to C_3 occur, increasing the mass fraction of ablated carbon. With increased temperature larger carbon vapor species sublime from the surface appearing first as species having from 4 to 10 carbon atoms and then in species having from 11 to 20 carbon atoms. For the 100-atm pressure condition shown, little contribution from vapor species with greater than 20 carbon atoms occurs. More clearly, than indicated in Figure 18, it is apparent that the additive small concentrations of the polyatomic carbon vapor species is quite appreciable.
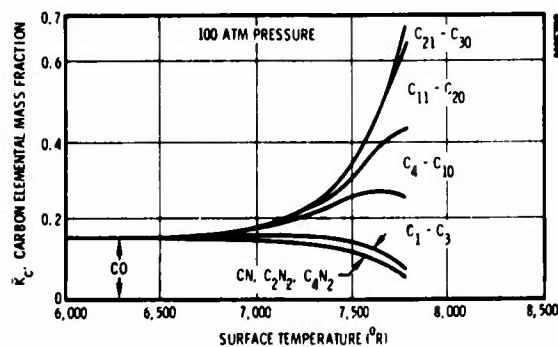
Figure 19. Partition of Elemental Mass Fraction of Carbon with Surface Temperature

Sensitivity Analysis

The uncertainty limits established for the carbon-vapor species as affects mass transfer and energy transfer can be assessed employing the conservation equations previously described. Figure 20 shows the normalized sublimation rate for several pressures including ±20% uncertainty in free energy of formation for the carbon-vapor species. The uncertainty band reflected in Figure 20 is consistent with the vapor pressure diagram shown in Figure 9; the higher pressure evidences a greater uncertainty band due to the greater concentration of sublimation species. For comparative purposes, results calculated by Scala[3] are shown for a normalized sublimation

11

rate of 4.0. Also shown, are results by Dolton et al. [14] at 1 atm pressure. He includes vapor species up to C_{16}, employing empirically determined free energies forced to fit a presumed 4,000°K triple-point temperature. It is seen that, at 100 atm pressure and for constant surface temperature, sublimation rate can be as much as 3 times larger than the nominal value. The effect of uncertainty in thermodynamic properties, diminishes with decreased pressure, owing to the smaller vapor-pressure contribution of the high molecular weight vapor products. Corresponding results showing the effect of the combustion-sublimation products on wall enthalpy, are shown in Figure 21. The composite of these results enable an assessment of the uncertainty on surface recession rate to be made.
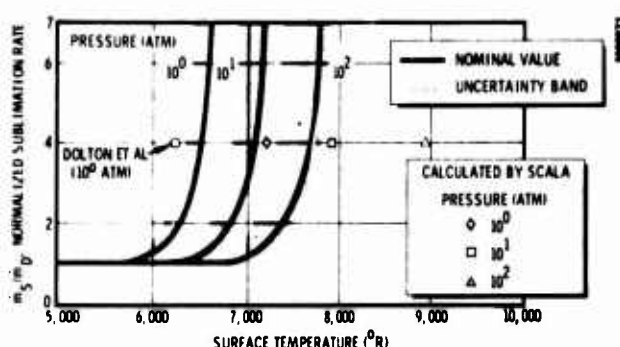

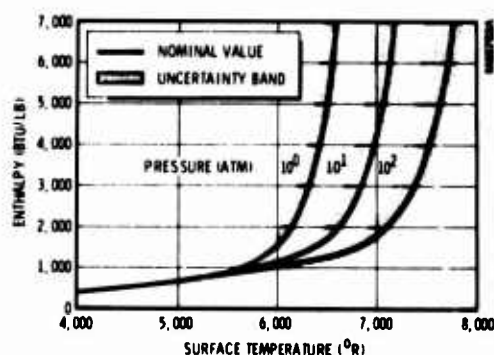Figure 20. Graphite Sublimation Rate Sensitivity to ±20% Uncertainty in ΔF_F^0

Figure 21. Sensitivity of Enthalpy of Combustion-Sublimation Products at Ablating Graphite Surface to ±20% Uncertainty in ΔF_F^0

The calculated surface recession rate for environmental conditions we have studied in correlation of high pressure test data is shown in Figure 22.
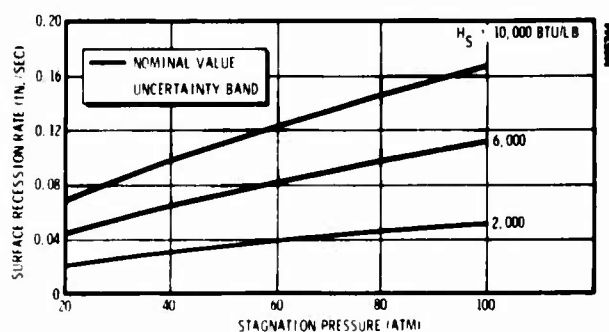

Figure 22. Thermochemical Surface Recession Rate

At the highest stagnation enthalpy shown (10,000 Btu/lb) calculated surface temperature is 7,500°R at 100 atm pressure. The sensitivity of surface recession, owing to the uncertainty band on properties, is small. This sensitivity decreases with both reduction in stagnation enthalpy and pressure, evidencing the effect shown in Figure 20 on sublimation rate. In the numerical results, we have obtained both transient and steady-state results, including loss of solid at the heated surface. In the transient calculations it was noted that the surface temperature approached a steady-state value in less than 0.1 second. For the most part, steady-state predictions were made to correlate the data because of the large numerical results required. Calculated surface temperatures including the effect of solid eroded is discussed subsequently in correlation of the arc jet data. Even though a large uncertainty in the thermodynamic properties of the carbon vapor species was included (resulting in almost a decade uncertainty in carbon-vapor pressure) the effect on surface recession is less than 10% within the environmental conditions discussed in this paper. This result occurs because of the counter-balancing effect of increased endothermic heat absorption when greater quantities of carbon vapor are evolved at the surface. Thus, when using a self-consistent model for calculating the vapor species thermodynamic properties with associated uncertainty, the sensitivity on surface recession is comparable to the accuracy for which local aerodynamic heating conditions can be defined.

V. Test Data and Analysis

The facility in which was gathered the majority of the data to be reported in this paper was the 1.5 MW arc heater test unit of the Propulsion Wind Tunnel Facility at AEDC in Tullahoma, Tenn. This facility uses the Linde N-4000 heater with an operational chamber pressure of 100 atmospheres maximum. The arc heater has two modes of operation in terms of the cathode. The short cathode, 26 inches in length, gives a bulk enthalpy of 3000 Btu per lb, and the long cathode, 34 inches in length, gives 2600 Btu per lb. Three nozzles were used during this test program; the first is a Mach 2.3 nozzle and yields stagnation pressure on the model of 55 atmospheres at a chamber pressure of 100 atmospheres. The second, a Mach 2.0 nozzle, yields 70 atmospheres on the model, and the third, a Mach 1.6 nozzle, yields 85 atmospheres on the model. A full description of the facility and its capability is given in Reference 42.

Conditions

The hemisphere-cone models were tested in the free jet configuration. The nozzle expansion ratios and chamber pressures were such that the free jet was always supersonic and highly underexpanded. The characterization of the test environment involved definition of the model flowfield, and model stagnation enthalpy and pressure. The jet flow field calibration is described in References 42 and 43, and thus only a brief summary will be given here. The high heating rate makes the design of instrumentation with sufficient response and longevity for making accurate measurements difficult. For this reason, measurement of heat flux and of other phenomena such as turbulence, pressure, and enthalpy profiles has not been attempted. It was found that the measured

values of heat flux did not agree with those predicted by Fay-Riddell [44] theory and any of the above unmeasured phenomena could contribute to this disagreement.

It is characteristic of the Linde N-4000 arc heater to produce a flow with a high enthalpy core; i.e., the centerline stagnation enthalpy of the jet is significantly greater than the average bulk enthalpy of the stream. Since insufficient evaluation of the turbulence or pressure gradients exists to allow quantitative assessment, the approach in this work has been to assume that the enthalpy profile is the source of the above-noted discrepancy.

To determine the magnitude of the centerline stagnation enthalpy of the jet, heat flux measurements were made using high response transient calorimeters. The apparent centerline stagnation enthalpy of the jet was then calculated using the stagnation point heating analysis, of Fay and Riddell. Figure 23 shows the correlation of apparent centerline stagnation enthalpy for the arc heater configurations used.
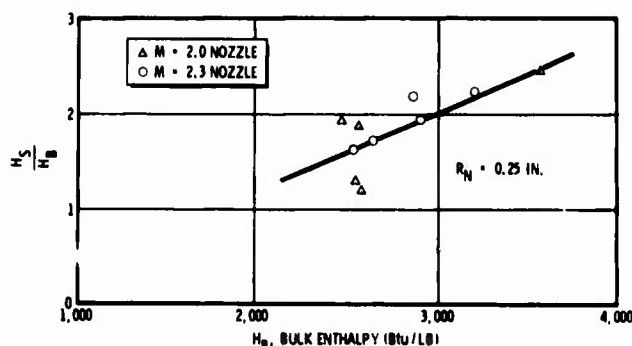

Figure 23. Ratio of Jet Centerline Stagnation Enthalpy to Bulk Enthalpy

Pertinent arc heater parameters were measured during each run to allow a heat balance determination of the average total (bulk) enthalpy of the flow. The total pressure of the flow was measured directly. The model flowfield could, therefore, be defined for each arc heater firing period. Ablation model data included surface brightness temperature measurements and high-speed (400 to 600 frames/second) motion picture coverage. Appropriate lenses and filters were used on the cameras to provide a large and clear representation of the ablating surface. All recorded data displays were correlated by an independent timing device. The test measurements and measurement techniques for the test program reported herein are given in Reference 45.

Data Reduction and Analysis

A total of 140 graphite models were tested at AEDC, including fine- and coarse-grain graphites. All of these models have rather small nose radii either 0.18 or 0.25 in. Surface temperature measurements were taken; however, difficulties were encountered. The problem lies not in the equipment available, but in the position in which this equipment must be placed in order to see the surface of the model. The model proximity to the jet exit is such that the pyrometers had to be placed at 90 degrees to the model centerline. Consequently, the pyrometer readings reflected an average temperature over the periphery of the model hemisphere nose and shoulder and are unacceptable for the stagnation point correlations presented here.

The recession rates have been determined from the motion picture coverage in order to obtain recession measurements after model warmup and before the model receded beyond the point where the total pressure began decreasing. A typical plot of data is shown in Figure 24. Experimental recession data in film reader units versus time from model injection are shown. The points represent individual measurements made from frames of the movie film. After a short warmup period the model evidenced linear recession and was apparently continuous. This is important, the linear recession indicated shows that the model rapidly approached steady state and that no major observable spallations occurred. The model recession rate determined is the slope of the linear portion of the data. As indicated, recession rates appear to decrease as the model recedes. This is caused by the total pressure decrease after passing from the "cone of silence." In reducing the data, recession rates are determined from the linear portion of the experimental data, thus avoiding the influence of nose blunting and decay in heat rate and pressure on recession rates as the model recedes.
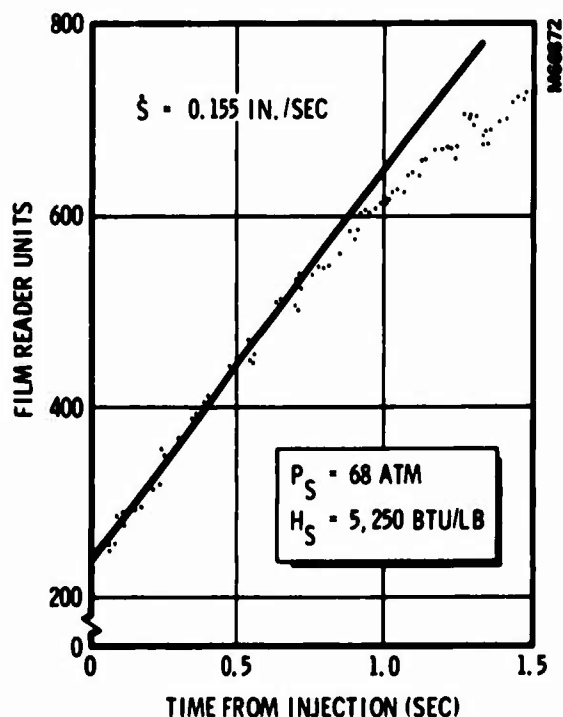

Figure 24. Typical Surface Recession History from Film Reading

A typical block of data reduced in this manner is shown in Figure 25; experimental recession data are plotted against apparent stagnation enthalpy. Two sets of data are given as typical. Shown are data taken in the stagnation pressure range of 83.5 to 88.6 atm and data gathered between 18.6 and 23.1 atm. Each set of data was correlated using a least squares curve fit of the data points. Results similar to these have been obtained for nominal stagnation pressures of 55 and 70 atm. In addition, recession data in the 6.5 to 9.8 atm range have been determined using data from Reference 46. The composite of the recession data enables construction of the experimental recession rate map shown in Figure 26. Here experimental recession rate is shown in terms of stagnation pressure and stagnation enthalpy. Figure 26 presents the total

picture of the dependency of the experimental recession rate data upon the environmental conditions, stagnation enthalpy, and pressure. The data appear to be linear functions of pressure and enthalpy.
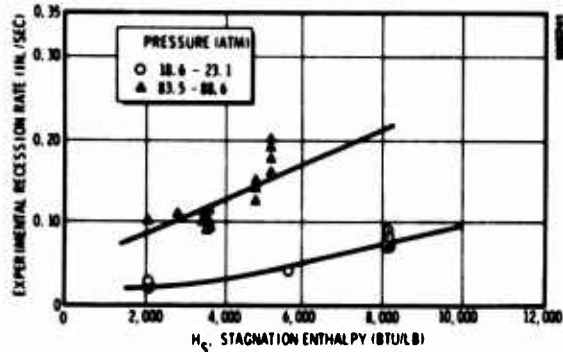

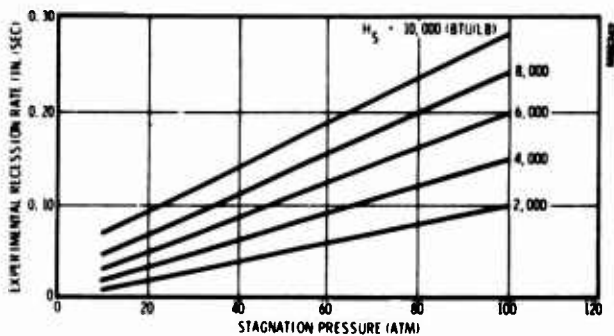Figure 25.   Experimental Recession Rate Data

Figure 26.   Experimental Recession Rate Data Map

Construction of the experimental recession data map enables a comparison of the calculated thermochemical recession to the observed experimental recession data. Figure 27 presents the ratio of experimental and thermochemical mass fluxes for the test environmental spectrum.
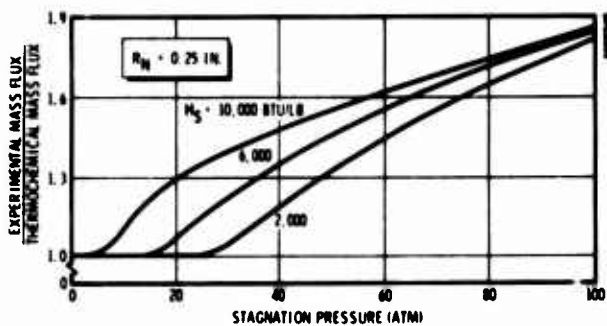

Figure 27.   Ratio of Experimental and Thermochemical Mass Fluxes

Thermochemical recession rates, including the uncertainty band in the carbon vapor properties, were given in Figure 22 for this environmental spectrum. For clarity, this uncertainty in thermochemical recession rates as affects the ratio given in Figure 27 is omitted (the ratio is affected by less than 10%). As indicated in Figure 27 the deviation from thermochemical recession is marked, being affected by both stagnation pressure and enthalpy. The experimental mass flux is about

a factor of 2 greater than that predicted by thermochemical erosion alone at 100 atm pressure. Complementary results are given in Figure 28 depicting the predicted surface temperature as affected by loss of solid from the heated surface. Noteworthy. is the rather small decrease in surface temperature for even large fractions of solid eroded. Surface temperature is most affected by solid loss at the low stagnation enthalpy; the high stagnation enthalpy somewhat masks the less efficient removal of material in the solid state.
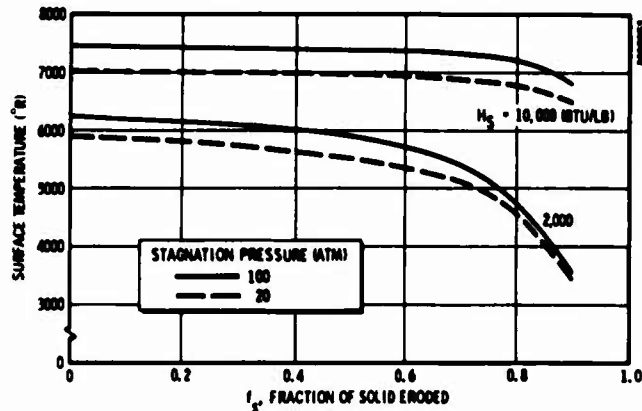

Figure 28.   Influence of Solid Fraction Eroded on Surface Temperature

Figure 29 shows the departure from thermochemical erosion in more meaningful terms. From the composite of experimental data (Figure 26) and numerical results, including solid removal, the fraction of solid eroded has been calculated and is depicted in Figure 29. Coincident with the results given in Figure 27 the threshold stagnation pressure at which loss of particulate solid initiates is dependent on stagnation enthalpy (reflecting convective heat rate at constant pressure). The results shown are consistent with those expected, increased stagnation enthalpy results in higher surface temperatures; hence, greater subsurface loss of binder material reducing binding of filler particles within the graphite matrix. Increasing pressure above the threshold value causes a large increase in the solid fraction eroded over a fairly narrow pressure range. The increment in solid eroded thereafter decreases as the full pressure range is covered.
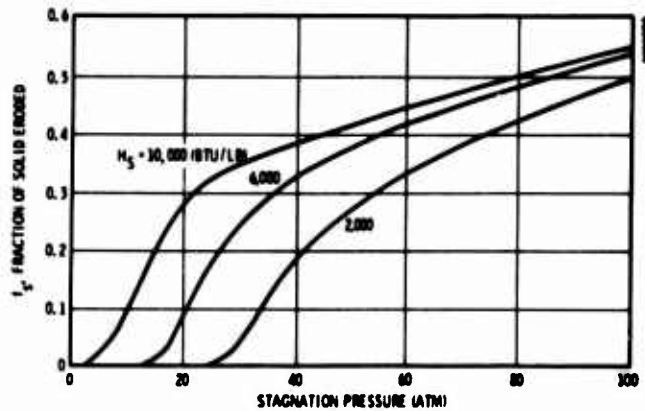

Figure 29.   Fraction of Solid Eroded from Experimental Data

To interpret the results in Figure 29 in terms of the contents of this paper reference is made to the postulated preferential erosion mechanism previously discussed. First, it was observed (Figure 28) that the effect of pressure on surface temperature is small at the respective values of stagnation enthalpy (within the pressure range covered). Thus, each value of stagnation enthalpy can be viewed in terms of nearly constant surface temperature for the range of solid fraction eroded evidenced in Figure 29. Consider then the role of stagnation pressure, the normal force acting on the heated surface. As the surface recedes, filler particles of various size are continuously exposed. Loss of binder below the heated surface and by direct thermochemical erosion at the surface tends to free the otherwise constrained and somewhat interlocked particles. The larger filler particles are then rather easily blown free by even moderate pressures, commencing with the higher temperature exposure conditions (i.e., stagnation enthalpy) with increased pressure acting to free the smaller particles. Also, minute amounts of binder leave the surface attached to the dislodged filler particles. As indicated in Figure 29 the effect of enthalpy (hence, surface temperature) at the higher pressures appears to diminish and pressure dominates the loss of particulate solid. Interestingly, the fraction of solid eroded appears to be approaching an asymptotic value in the range 0.6 to 0.8. Significantly, the nominal mass fraction of filler particles (about 0.75) falls within this range. Finally, the effect of aerodynamic shear and pressure gradients typical of positions removed from the stagnation point is to induce increased particle loss. Thus, one is faced with loss of particulate graphite over a rather broad range of aerodynamic conditions, perhaps even extending into the relatively moderate super-orbital entry environment.

VI. Conclusions

A model incorporating the allotropic features of bulk graphite has been postulated and used to describe the continuous removal of particulate graphite from the heated surface. Although hypothetical in its formation, sufficient laboratory data and pre- and post-test arc-jet data are advanced to establish the creditability of removal of filler particles in the solid state. The key role of the different forms of carbon in graphite on surface erosion has been established. Thermodynamic properties of the linear and cyclic molecules C_3 to C_{30} were calculated by quantum and statistical mechanical techniques. The resonance energy of each molecule was computed from the respective electronic wave functions, and the corresponding vibrational frequencies were determined by a normal coordinate analysis of the molecular structure. The theoretical procedures are self-consistent, resort to the empirical increments adopted by Pitzer and Clementi and used by others has been avoided. The agreement of the calculated vapor pressure with the triple-point and sublimation data is excellent. By purely analytical means, the uncertainty in the free energy of formation has been established; the effect on calculated thermochemical surface recession was found to be small. Significantly, this result has enabled identification of the solid fraction of graphite eroded in high-pressure ground tests with confidence.

To establish the solid fraction of particulate graphite eroded ablation data encompassing fine to coarse grain graphites have been correlated. The loss of material in the solid state has been determined over a range of environmental conditions (in terms of stagnation pressure and enthalpy) evidencing large fractions of solid removal. Loss of particulate solid initiates at rather low stagnation pressures; the actual threshold is dependent on heating rate as well as pressure. The mechanism by which loss of particulate graphite occurs appears to be by preferential surface recession and subsurface loss of binder phase, freeing the filler particles from the binder matrix. Filler particles are then easily dislodged from the surface by even moderate forces (i.e., pressure, shear). Surprisingly, the loss of solid at the heated surface does not appreciably depress surface temperatures, even for rather large fractions of solid loss.

The results presented in this paper open several interesting avenues for pursuit. Clearly, the role of graphite microstructure in dictating surface erosion cannot be dismissed. Closely related to the microstructure of the binder and filler phases are the thermophysical, mechanical, and chemical properties which individually, or in combination, affect ablation performance. Future analyses employing statistical distributions of particle size, void size and spacing, and accounting for the temperature-time course of the crystallite growth will be necessary before a completely analytical performance description of graphite can be achieved. Finally, new graphites overcoming the evident dissimilar characteristics of the constituent materials appear to afford a means of reducing or alleviating preferential erosion, hence, loss of solid material.

VII. Acknowledgment

VIII. References

1. Bishop, W. M. and DiCristina, V., "A Prediction Technique for Ablative Material Performance Under High Shear Re-Entry Conditions," AIAA Journal, Vol. 6, No. 1, Jan. 1968.

2. Bishop, W. M., and DiCristina, V., "The Combustion and Sublimation of Carbon at Elevated Temperatures," AIAA Paper 68-759, June 1968.

3. Scala, S. M. and Gilbert, L. M., AIAA Journal, 3, 1635 (1965).

4. Moyer, C. B. and Rindal, R. A., "Finite Difference Solution for the In-Depth Response of Charring Materials Considering Surface Chemical and Energy Balances," Aerotherm Corporation Final Report No. 66-7, Part II, March 1967.

5. Kratsch, K. M., Hearne, L. F., and McChesney, H. R. "Thermal Performance of Heat Shield Composites During Planetary Entry." Presented at the American Institute of Aeronautics and Astronautics - National Aeronautics and Space Administration National Meeting, Palo Alto, Calif., September 30-October 1, 1963, reprinted in Engineering Problems of Manned Interplanetary Exploration, American Institute of Aeronautics and Astronautics, New York, 1963.

6. Scala, S. M. and Gilbert, L. M., "Thermal Degradation of a Char Forming Plastic During Hypersonic Flight," ARS Journal, Vol. 32, No. 6, June 1962, pp. 917-924.

7. Mathieu, R. D., "Mechanical Spallation of Charring Ablators in Hyperthermal Environments," AIAA Journal, Vol. 2, No. 9, Sept. 1964, pp. 1621-1627.

8. Schneider, P. J., Dolton, T. A., and Reed, G. W., AIAA Journal, 6, 64 (1968).

9. Mrozowski, S., "Mechanical Strength, Thermal Expansion and Structure of Cokes and Carbons," Proceedings of the First and Second Conference on Carbon, 1956.

10. Riley, W. C., "Graphite," High Temperature Materials and Technology, John Wiley and Sons, Inc., 1967.

11. Wachi, F., Private communication (Aerospace Corp., El Segundo, Calif. 1968).

12. Pitzer, K. S., and Clementi, E., J. Am. Chem. Soc., 81, 4477 (1959).

13. Duff, R. E., and Bauer, S. H., J. Chem. Phys., 36, 1754 (1962).

14. Dolton, T. A., Maurer, R. E., and Goldstein, H. E., AIAA 3rd Thermophysics Conference, Paper No. 68-754, Los Angeles, California, June, 1968.

15. Basset, J., Chemie and Industrie, 45, No. 3f, 7 (1941).

16. Scala, S. M., and Gilbert, L. M., "The Sublimation of Graphite at Hypersonic Speeds," General Electric Co. Missile and Space Division, R64SD55, Aug, 1964.

17. McChesney, H. R., "Sublimation Energy and Vapor Equation of State for Graphite," Lockheed Missiles and Space Co., Dec. 31, 1963.

18. Krieger, F. J., "Thermodynamics of the Graphite-Carbon Vapor System," The Rand Corp., RM 3326 PR, September, 1962.

19. Baun, W. L., and Fisher, D. W., J. Chem. Phys., 35, 1518 (1961).

20. Dörnenburg, E., Hintenberger, H., and Franzen, J., Z. Naturfursch, 16a, 532 (1961).

21. Strickler, S. J., and Pitzer, K. S., "Molecular Orbitals in Chemistry, Physics, and Geology," P. Löwdin, Ed., Academic Press, New York, 1964.

22. Herzberg, G., "Molecular Spectra and Molecular Structure, Vol. III: Electronic Spectra and Electronic Structure," D. Van Nostrand Co., Princeton, New Jersey, 1966.

23. Livingston, R. L., and Rao, C. N., J. Am. Chem. Soc., 81, 285, (1959).

24. Drowart, J., Burns, R. P., DeMaria, G., and Inghram, M. G., J. Chem. Phys., 31, 1131 (1959).

25. Hoffmann, R., J. Chem. Phys., 39, 1397 (1963).

26. Hoffmann, R., Tetrahedron, 22, 521 (1966).

27. Moore, C. E., "Atomic Energy Levels," Circular of the National Bureau of Standards 467, Vol. I, U. S. Government Printing Office, Washington, D. C., 1949.

28. Altman, R. L., J. Chem. Phys., 32, 615 (1960).

29. Clementi, E., Astrophys. J., 133, 303 (1961).

30. JANAF Thermochemical Data, Dow Chemical Company, Thermal Laboratory, Midland, Michigan.

31. Gausset, L., Herzberg, G., Lagerqvist, A., and Rosen, B., Astrophys. Journal, 142, 45 (1965).

32. Smith, W. H., and Leroi, G. E., J. Chem. Phys., 45, 1767 (1966).

33. Smith, W. H., and Leroi, G. E., J. Chem. Phys., 45, 1784 (1966).

34. Lord, R. C., and Andrews, D. H., J. Phys. Chem., 41, 149 (1937).

35. Thorn, R. J., and Winslow, G. H., J. Chem. Phys., 26, 186 (1957).

36. Schoessow, G. J., "Graphite Triple Point and Solidus-Liquidus Interface Experimentally Determined up to 1000 Atmospheres, College of Engineering, University of Florida, Dec. 1967.

37. Fateeva, N. I. et al., Doklady Akademic Nauk SSSR, 152, No. 1, 1963.

38. Lees, L., "Convective Heat Transfer With Mass Addition and Chemical Reactions," Third AGARD Combustion and Propulsion Colloquium, May 1958.

39. Dorrance, W. H., "Viscous Hypersonic Flow," McGraw-Hill Series in Missile and Space Technology, 1962 ed.

40. Kendall, R. M., Bartlett, E. P., Rindal, R. A., and Moyer, C. B., "An Analysis of the Coupled Chemically Reacting Boundary Layer and Charring Ablator," NASA CR-1060, June 1968.

41. Hearne, L. F., Gallagher, L. W., and Woodruff, L. W., "Surface Oxidation with Streamwise Variation of Wall Reactivity," AIAA 3rd Thermophysics Conference, Paper No. 68-755, Los Angeles, California, June 1968.

42. Test Facilities Handbook (Sixth Edition). "Propulsion Wind Tunnel Facility," Vol. 5, Arnold Engineering Development Center, November 1966.

43. Fisher, E. B., "Free Jet Calibration Tests Conducted on the AEDC 5-Megawatt Arc Heater Test Unit," Cornell Aeronautical Laboratory Report No. AH-2243-W-1, August 1966.

44. Fay, J. A., and Riddell, F. R., "Theory of Stagnation Point Heat Transfer in Dissociated Air," J. Aerosci. 25, No. 2, Feb 1958.

45. Private communication to author.

46. Sallis, D. V., et al., "Evaluation of Ablative Materials," Technical Report AFML-TR-66-348, September 1967.